

Composition Change of Stainless Steels during Keyhole Mode Laser Welding

The experimental and theoretical study of composition changed during keyhole mode welding of stainless steels

T. LIU, L. J. YANG, H. L. WEI, W. C. QIU, AND T. DEBROY

ABSTRACT

Vaporization of alloying elements during laser beam welding adversely affects weld metal composition and properties. Alloying element vaporization and weld metal composition change during partial and complete joint penetration keyhole mode Nd:YAG laser welding of two stainless steels containing different concentrations of manganese were examined experimentally and theoretically. The keyhole and weld pool geometry and the temperature field were computed from a well-tested, three-dimensional heat transfer and fluid flow model, and the results were used in a model for the calculation of weld metal composition change based on the principles of transport phenomena, kinetics, and thermodynamics. The results showed that vaporization from the keyhole was the most pronounced source of alloying element loss for all welding conditions. The weld metal composition was spatially homogeneous, but the concentration of manganese decreased while the concentration of iron slightly increased for all welding conditions. The change in the weld metal composition was much more pronounced for the higher manganese steel. The change in the weld metal composition was much more sensitive to laser power than welding speed for both partial and complete joint penetration welds.

KEYWORDS

• Composition Change • Vaporization • Keyhole • Laser Welding • Stainless Steel

Introduction

Laser welding is widely used in aerospace, automotive, and other manufacturing industries owing to its deep penetration, excellent precision, high productivity, and amenability to automation. Because of the high power density used, the weld metal is rapidly heated to very high temperatures and a keyhole filled with metal vapors is formed directly under the laser beam. The formation of the keyhole is accompanied by significant vaporization of various volatile alloying elements, not all of which vaporize at the same rate. Apart from the keyhole, vaporization also occurs from the surface of the weld pool. The loss of alloying elements results in an undesirable change in the weld metal composition as well as degradation of

the mechanical and corrosion properties of the weld. In the electronics industry, components are often processed in clean rooms where emission of metal vapors is not acceptable.

Selective vaporization of alloying elements from the weld pool at relatively low power densities have been studied before because of its detrimental effects. For example, the hardness of aluminum alloy weld metal was found to be lower than that of the base metal due to vaporization of magnesium and the reduction of solid solution strengthening (Ref. 1). Most of the previous research on alloying element vaporization was focused on either isothermal systems or at relatively low laser power densities where the keyhole did not form. For example, Anisimov and Rakhmatulina (Ref. 2)

and Knight (Refs. 3, 4) derived a set of gas dynamic equations for the vapor temperature, density, velocity, and the extent of the condensation across the Knudsen layer by solving the equations of conservation of mass, momentum, and energy for the vaporization from isothermal surfaces.

Mundra and DebRoy (Ref. 5) proposed a model to calculate the vaporization rate and composition change of stainless steel in conduction mode laser welding. Similarly, Zhao and DebRoy (Ref. 6) and He et al. (Ref. 7) computed vaporization rates and composition changes in aluminum alloy and stainless steel during conduction mode Nd:YAG laser welding, respectively. As a result of the previous work (Refs. 1–13), the composition change and its detrimental effects are now well recognized for conduction mode laser welding. However, very little work has been done on the alloying element loss and composition change due to selective vaporization of alloying elements during keyhole mode laser welding.

Keyhole mode laser welding is much more complex than conduction mode welding. Pronounced vaporization of alloying elements is a requirement for the stability of the keyhole. The distribution of power density, laser beam radius and profile, welding speed, specimen thickness, and the nature of the alloy affect the geometry of the keyhole, its stability, weld pool temperature distribution, and the recirculating flow of liquid metal within the moving weld pool. The vaporization rates of alloying elements depend on the shape and size of the keyhole as well as its wall temperature. They are also affected by welding parameters

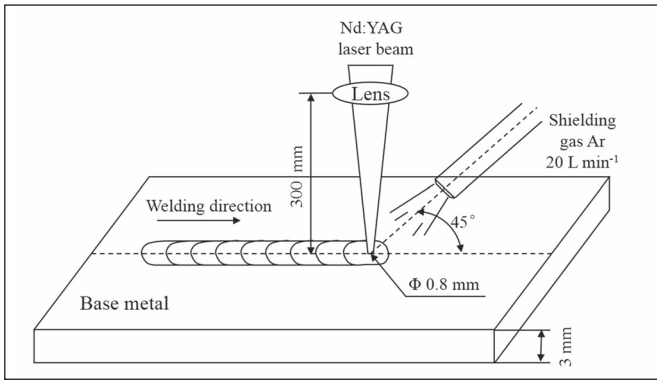


Fig. 1 — Schematic representation of the experimental setup.

and alloy properties. Because of these complexities, several simplifying assumptions have been made in the past to understand the alloying element vaporization during keyhole mode welding. For example, Dilthey et al. (Ref. 14) developed a model to calculate the composition change in keyhole mode CO₂ laser welding. The keyhole was considered as a cylinder for simplicity around which the liquid metal circulated within the weld pool. Jandaghi et al. (Refs. 15, 16) studied the composition change in 5754 aluminum alloy and 316 stainless steel during pulsed Nd:YAG laser welding. However, the temperature fields were obtained from a simplified heat conduction model that ignored convective heat transfer. It is well known that this practice results in significant errors (Ref. 17).

The keyhole shape and size, the geometry of the weld pool, and the temperature field in the weld pool affect the vaporization behavior. Vaporization occurs from both within the keyhole and the top surface of the weld pool. Rigorous calculations of both are necessary to quantitatively understand the alloying element loss during keyhole mode laser welding. A detailed experimental and theoretical study of the vaporization behavior during keyhole mode laser welding has not been reported.

Here we present an experimental and theoretical investigation of the loss of alloying elements and weld metal composition change during partial and complete joint penetration keyhole mode

Nd:YAG laser welding of two varieties of stainless steel containing different concentrations of manganese. A well-tested, comprehensive, keyhole mode heat transfer and fluid flow model was used to understand the keyhole shape and size as well as temperature field. Spatial variations of the concentrations of iron, manganese, chromium, and nickel in the weld metal were examined by electron probe microanalysis (EPMA) after welding. The experimentally determined weld pool geometry and the change in the composition of the alloying elements for various welding speeds were compared with the corresponding model predictions.

Experimental Procedure

A schematic diagram of the experimental setup is shown in Fig. 1. Bead-on-plate Nd:YAG laser welds on 3.0-

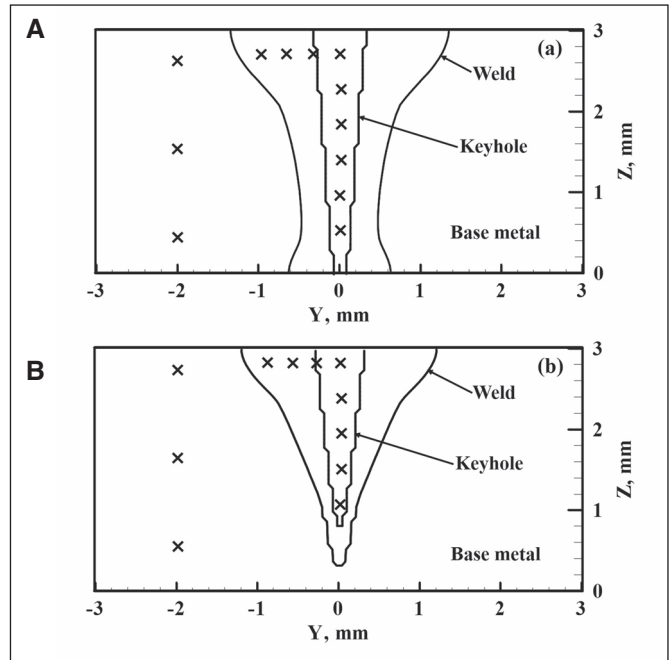


Fig. 2 — Schematic representation of the locations where the chemical composition was determined by EPMA: A — Complete joint penetration welds; B — partial joint penetration welds.

mm-thick stainless steel plates were studied. The compositions of two types of stainless steel, 204 (204 SS) and 304 (304 SS), containing different concentrations of manganese and other alloying elements are presented in Table 1. The plate surface was polished with sand paper to remove the oxide skin and cleaned in ethyl alcohol before welding.

Keyhole mode welding was performed using a continuous wave Nd:YAG laser (GSI JK2003M) having a wavelength of 1064 nm. The laser beam was focused on the specimen surface using a 300-mm focal length lens. The focal spot of the laser beam was 0.8 mm in diameter. The laser beam parameters were from the manual of the equipment. The defocusing distance was 0 mm for all the experiments. Laterally injected argon was supplied as the shielding gas through a 6-mm-diameter gas nozzle at a flow rate of 20 L min⁻¹ to

Table 1 — Compositions of the Stainless Steels wt-%

Alloying Elements	Mn	Cr	Ni	Si	C	P	S	Fe
204 SS	10.5	14.0	1.3	0.45	≤0.05	≤0.04	≤0.03	balance
304 SS	1.2	19.2	6.5	0.77	≤0.05	≤0.04	≤0.03	balance

Table 2 — EPMA Results of Elements Concentration in Various Conditions

Material	Laser Power/W	Welding Speed/mm s ⁻¹	Average Weight Percent (deviation)				
			Mn	Ni	Cr	Fe	
204 SS	base metal		10.437 (0.261)	1.288 (0.047)	14.064 (0.059)	72.992 (0.283)	
		1200	8	9.112 (0.217)	1.326 (0.001)	14.210 (0.036)	74.247 (0.046)
		1250	8	9.265 (0.059)	1.314 (0.012)	14.203 (0.045)	74.041 (0.132)
		1300	8	9.489 (0.078)	1.324 (0.008)	14.201 (0.021)	73.656 (0.095)
		1350	8	9.549 (0.166)	1.305 (0.007)	14.174 (0.041)	73.868 (0.079)
		1300	6	9.350 (0.079)	1.319 (0.012)	14.164 (0.005)	73.875 (0.382)
		1300	8	9.489 (0.078)	1.324 (0.008)	14.201 (0.021)	73.656 (0.095)
		1300	12	9.442 (0.102)	1.308 (0.010)	14.178 (0.001)	73.825 (0.123)
		304 SS	base metal		1.205 (0.043)	6.526 (0.300)	19.225 (0.158)
1250	8			1.080 (0.024)	6.569 (0.004)	19.046 (0.054)	72.793 (0.055)

avoid oxidation. As shown in Fig. 1, the angle of the gas nozzle was 45 deg to the horizontal plane, and the distance between the laser spot and the nozzle was about 20 mm. The variables studied were laser power in the range of 1200 W to 1350 W and welding speed between 6 to 12 mm s⁻¹.

After welding, the specimens were cut to obtain the transverse cross sections using wire electrical discharge machining, and prepared using the standard polishing technique. The concentrations of manganese, chromium, nickel, and iron in both the base metal and the weld metal were determined by EPMA. The EPMA was performed by using a CAMECA SXFive with an accelerating voltage of 20 KeV and a beam current of 100 nA. The K_α lines of manganese, chromium, nickel, and iron were measured with the standards of manganese metal, chromium metal, nickel metal, and cast iron and NIST 363 steel, respectively.

The concentrations of alloying elements were determined before and after the experiments in at least 11 locations on the transverse cross sections as shown in Fig. 2. The average concentrations of each alloying element and their standard deviations are shown in Table 2.

Table 3 — Data Used for Calculations

Property/Parameter	204 SS	304 SS
Density of liquid metal (kg m ⁻³)	7.80 × 10 ³	7.20 × 10 ³
Absorption coefficient	0.22	0.22
Effective viscosity (kg m ⁻¹ s)	0.1	0.1
Solidus temperature (K)	1787	1697
Liquids temperature (K)	1811	1727
Enthalpy of solid at melting point (J kg ⁻¹)	1.2 × 10 ⁶	1.2 × 10 ⁶
Enthalpy of liquid at melting point (J kg ⁻¹)	1.26 × 10 ⁶	1.26 × 10 ⁶
Specific Heat of solid (Jkg ⁻¹ k)	710.6	711.8
Specific Heat of liquid (Jkg ⁻¹ k)	836.0	837.5
Thermal conductivity of solid (J m ⁻¹ s K)	19.26	19.26
Thermal conductivity of liquid (J m ⁻¹ s K)	20.93	20.93
Temperature coefficient of surface tension (N m ⁻¹ K)	-4.3 × 10 ⁻⁴	-4.3 × 10 ⁻⁴
Coefficient of thermal expansion (K ⁻¹)	1.96 × 10 ⁻⁵	1.96 × 10 ⁻⁵

Mathematical Modeling

Heat Transfer in the Weld Pool

The temperature and velocity fields, keyhole geometry, and fusion zone geometry were calculated from a well-tested, 3D, steady-heat transfer and fluid flow model (Refs. 18–20). The data used for the calculations (Refs. 5, 7) are presented in Table 3. The assumptions, governing equa-

tions, boundary conditions, and their solution for the keyhole mode welding have been described in previous papers (Refs. 18–22). The salient features of the model are provided in Appendix A. The computed geometry of the keyhole and the weld pool and the temperature field were used for the calculation of the alloying element vaporization and composition change as described below.

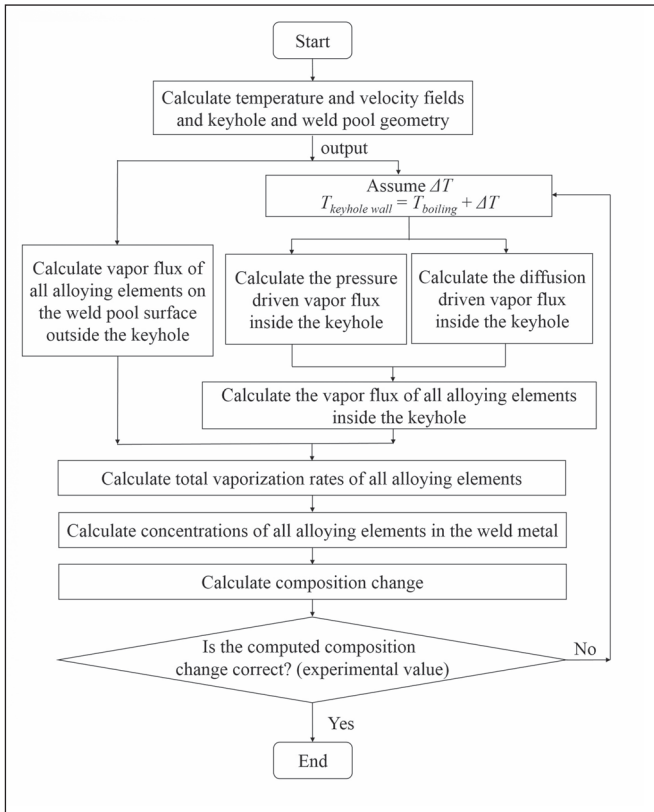


Fig. 3 — A flow chart for the calculation of vaporization rates and composition change during keyhole mode laser welding.

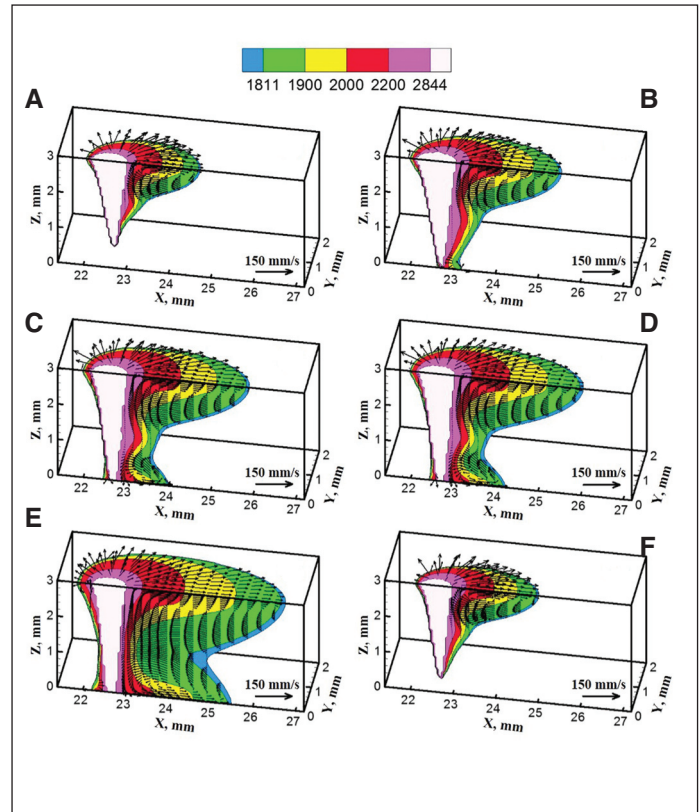


Fig. 4 — Computed temperature and velocity fields for different welding parameters: A — $P = 1200\text{ W}$, $v = 8\text{ mm s}^{-1}$; B — $P = 1250\text{ W}$, $v = 8\text{ mm s}^{-1}$; C — $P = 1300\text{ W}$, $v = 8\text{ mm s}^{-1}$; D — $P = 1350\text{ W}$, $v = 8\text{ mm s}^{-1}$; E — $P = 1300\text{ W}$, $v = 6\text{ mm s}^{-1}$; and F — $P = 1300\text{ W}$, $v = 12\text{ mm s}^{-1}$.

Driving Forces for Vaporization

The metal vapors exit from the keyhole to keep it open during the welding process. The pressure inside the keyhole is slightly higher than the ambient pressure. The overpressure provides the main driving force for the metal vapor to escape from the keyhole. Furthermore, the concentrations of the alloying elements in the vapor within the keyhole are considerably higher than those outside the keyhole. Therefore, the flow of metal vapor out of the keyhole is driven by the concentration gradients. In addition to the keyhole, vaporization also occurs from the surface of the weld pool similar to conduction mode laser welding.

If equilibrium is attained on the keyhole surface, the keyhole wall temperature needs to slightly exceed the boiling point of the alloy for the equilibrium vapor pressure on the keyhole wall to be greater than the ambient pressure. The excess pressure provides a driving force for the vapor to move out from the keyhole wall. Close to the surface of the keyhole wall, there is a space of several mean-free-paths

length, known as the Knudsen layer (Ref. 3). Theoretical calculations of the vaporization rates in the Knudsen layer is based on treating this region as a gasdynamic discontinuity. Anisimov and Rakhmatulina (Ref. 2) and Knight (Ref. 4) derived expressions for the vapor temperature, density, velocity, and the extent of the condensation across the Knudsen layer by solving the equations of conservation of mass, momentum, and translational kinetic energy. A brief account of the calculation of the vaporization flux, J_p , owing to the pressure gradient on the pool surface is provided in Appendix B. The vaporization rate can be calculated from the following expression (Refs. 5–10):

$$J_p = \rho_v MS \tag{1}$$

where ρ_v is the density of the vapor at the edge of the Knudsen layer, and M and S are the Mach number and speed of sound in the vapor, respectively. The vaporization flux of an alloying el-

ement i , $J_{p,i}$, from the pressure gradient can be obtained from the following relation (Ref. 10):

$$J_{p,i} = a_i \frac{P_i^0}{P_i} \frac{M_i}{M_v} J_p \tag{2}$$

where a_i is the activity of the element i in the liquid metal, which is determined by its concentration in the weld pool. In this calculation, the mole fraction of the element i was used as the value of a_i because alloys behave ideally close to their boiling points. P_i^0 is the equilibrium vapor pressure of element i over pure liquid, P_i is the equilibrium vapor pressure over the alloy, M_i and M_v are the molecular weight of element i , and the average molecular weight of the vapor, respectively.

The concentrations of metal vapors at the keyhole wall and weld pool surface differ from those in the bulk gas phase. These differences provide driving forces for diffusive flux of alloying elements, $J_{c,i}$, which is given by the fol-

lowing expression (Ref. 10):

$$J_{c,i} = K_{g,i} \left(M_i \frac{a_i P_i^0}{RT_l} - C_i^b \right) \quad (3)$$

where $K_{g,i}$ is the mass transfer coefficient of element i , R is the gas constant, T_l is the temperature at the edge of the Knudsen layer, C_i^b is the concentration of element i in the shielding gas. The concentrations of alloying elements in the shielding gas, C_i^b is negligible. The mass transfer coefficient, $K_{g,i}$, between the weld pool surface and the shielding gas can be deduced from the graphical results of Schlunder and Gnielinski (Ref. 23) for a jet impinging on a flat surface:

$$K_{g,i} = \frac{2Sc_i^{0.42} Re^{0.5} D_i}{d} \left(1 + \frac{Re^{0.55}}{200} \right)^{0.5} \left[0.483 - 0.108 \frac{r}{d} + 7.71 \times 10^{-3} \left(\frac{r}{d} \right)^2 \right] \quad (4)$$

where d is the diameter of the nozzle, r is the radial distance on the pool surface, D_i is the average diffusivity of the element i in the shielding gas, Re is the Reynolds number at the nozzle exit, and Sc_i is the average Schmidt number of the element i and is defined as the ratio of kinematic viscosity of the shielding gas and the average diffusivity of element i in the shielding gas.

Composition Change in the Keyhole Mode Weld Pool

In this calculation, the temperature of the keyhole wall is assumed to be constant and slightly higher than the boiling point, which is iterated to obtain good agreement with the experimental data. For the conditions of all experiments, a value of 10 K for 204 stainless steel and a value of 9 K for 304 stainless steel above the boiling points resulted in good agreement of the computed and the experimentally determined weld metal compositions. The vapor flux from the keyhole, $J_{k,i}$, is the sum of the diffusion driven flux $J_{c,i}$, and the pressure driven flux, $J_{p,i}$ and is given by

$$J_{k,i} = J_{p,i} + J_{c,i} \quad (5)$$

However, the vapor flux from the weld pool surface, $J_{s,i}$, is only driven by the diffusion, which is given by

$$J_{s,i} = J_{c,i} \quad (6)$$

The geometry of the keyhole wall and the surface of the weld pool can be computed from the heat transfer and fluid flow model. Then, the vaporization rate of element i , G_i is obtained by

integrating the vapor flux from both the keyhole wall and the weld pool surface. The total vaporization rate, G , is given by

$$G = \sum_{i=1}^n G_i = \sum_{i=1}^n \iint_{Sk} J_{k,i} dx dy + \sum_{i=1}^n \iint_{Ss} J_{s,i} dx dy \quad (7)$$

where Sk and Ss denote the internal surface area of the keyhole wall and the area of the weld pool top surface outside the keyhole, respectively.

The final concentration of element i

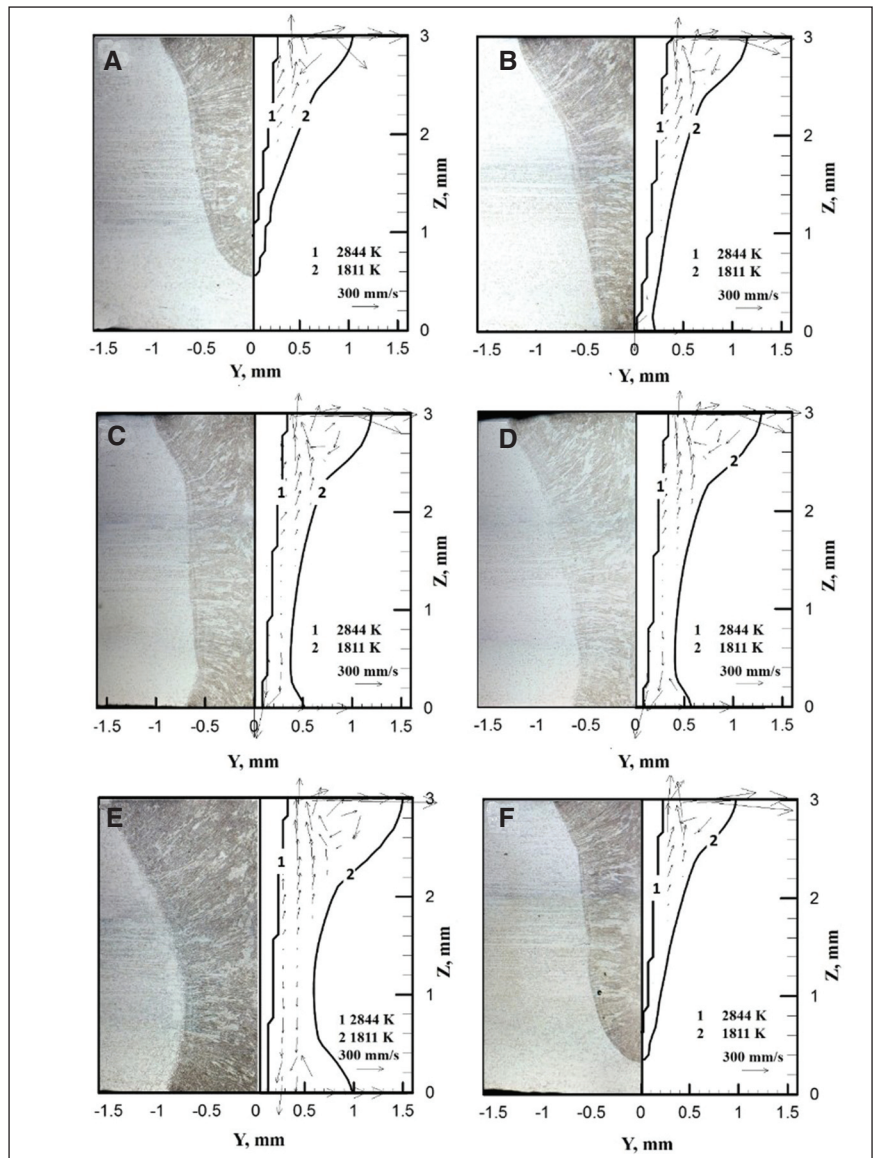


Fig. 5 — Experimental and calculated weld pool transverse cross sections for various welding parameters: A — $P = 1200$ W, $v = 8$ mm s^{-1} ; B — $P = 1250$ W, $v = 8$ mm s^{-1} ; C — $P = 1300$ W, $v = 8$ mm s^{-1} ; D — $P = 1350$ W, $v = 8$ mm s^{-1} ; E — $P = 1300$ W, $v = 6$ mm s^{-1} ; F — $P = 1300$ W, $v = 12$ mm s^{-1} .

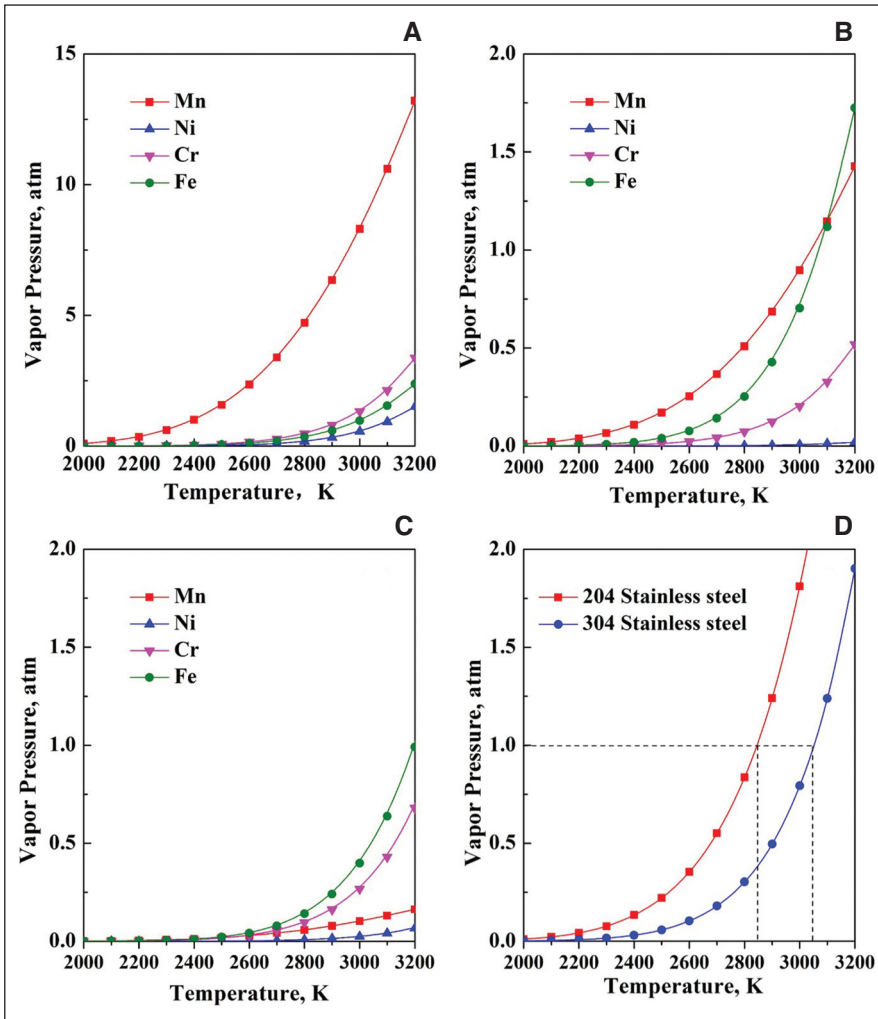


Fig. 6 — Equilibrium vapor pressures of the various alloying elements over the following: A — Respective pure liquids; B — liquid 204 stainless steel; C — liquid 304 stainless steel; D — total vapor pressures as a function of temperature.

after welding, C_i , is given by:

$$C_i = \frac{\rho v A C_{b,i} - G_i}{\rho v A - G} \tag{8}$$

where ρ is the density of the liquid metal, v is the welding speed, A is the transverse cross section area of the weld, and $C_{b,i}$ is the concentration of element i in the base metal. Then the composition changes are calculated by:

$$\Delta C_i = C_i - C_{b,i} \tag{9}$$

The steps involved in the calculation of the vaporization rate and composition change during keyhole mode laser welding are presented as a flow chart in Fig. 3.

Results and Discussion

Temperature Field and Weld Pool Geometry

Figure 4 shows the computed temperature and velocity fields at the top surface and the symmetry plane of the welds for various laser powers and welding speeds. The boiling point contours mark the keyhole boundary whereas the solidus isotherms indicate the weld pool periphery. On the top surface of the molten pool, the molten metal flows outward from the middle to the periphery driven by the Marangoni force, which results from the spatial variation of the surface tension owing to the temperature gradient. The velocities decrease and the weld pool narrows below the top sur-

face. Due to the motion of the laser beam, the temperature contours are compressed in the front of the heat source and elongated behind it.

Note that complete joint penetration welds are achieved for the power and speed indicated in Fig. 4B, C, D, and E, while partial joint penetration welds are obtained for the welding conditions in Fig. 4A and F. For the complete joint penetration welds, the weld pool extends to the bottom surface, and a flow pattern of liquid metal similar to that at the top surface is attained because of the Marangoni force. The weld pool is wider both on the top and bottom surfaces and narrower in the middle.

The maximum velocities of the liquid metal in the molten pool for various welding conditions shown in Fig. 4 are roughly 150 mm s^{-1} , and at these velocities convection is the dominant mechanism of heat transfer. The importance of heat transfer by convection relative to heat transfer by conduction can be determined by the Peclet number, P_e , which is given by

$$P_e = \frac{\mu \rho C_p L}{k} \tag{10}$$

where μ is the characteristic velocity, ρ is the density, C_p is the specific heat, L is the characteristic length, and k is the thermal conductivity. Using $\mu = 0.15 \text{ m s}^{-1}$, $\rho = 7800 \text{ Kg m}^{-3}$, $C_p = 836.0 \text{ J kg}^{-1} \text{ K}^{-1}$, $L = 1.0 \times 10^{-3} \text{ m}$, and $k = 20.93 \text{ J m}^{-1} \text{ s}^{-1} \text{ K}^{-1}$, $P_e = 46.7$. This value of Peclet number indicates that convective heat transfer is the dominant mechanism of heat transfer within the weld pool.

Figure 5 shows the experimental and calculated weld pool transverse sections for various welding parameters. A wide fusion zone on the top surface is produced due to the convective heat transfer within the molten pool. For the complete joint penetration welds, the fluid flow pattern on the bottom surface is similar to that on the top surface, and the widening of the fusion zone is also observed. The computed weld pool geometry is in fair agreement with the corresponding experimental results for all the welding conditions.

Vaporization and Composition Change

Figure 6A shows the computed va-

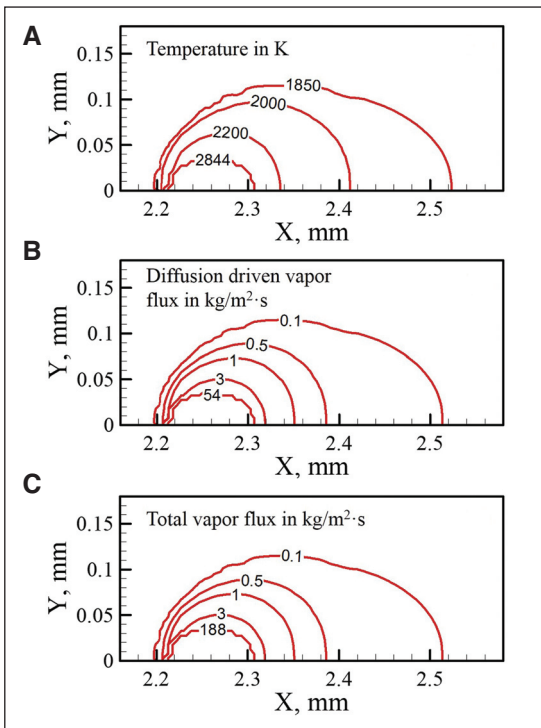


Fig. 7 — Temperature field and the vapor fluxes on the top surface of the weld pool for 204 stainless steel. $P = 1250\text{ W}$, $v = 8\text{ mm s}^{-1}$.

por pressures of various alloying elements over their pure liquids at various temperatures. It can be seen that the equilibrium vapor pressure of manganese is higher than those of chromium, iron, and nickel. Assuming that the molten steels behave as ideal solutions, the equilibrium vapor pressures of alloying elements over the 204 stainless steel liquid steel is obtained by multiplying the vapor pressures of Fig. 6A by their respective mole fractions. These values are shown in Fig. 6B as a function of temperature. The equilibrium vapor pressure of iron is higher than that of manganese when the temperature exceeds 3100 K because of its high mole fraction of iron.

The boiling points of the alloys are determined by computing the equilibrium vapor pressures of the alloying elements over the liquid alloys as a function of temperature and determining the temperature at which the sum of the equilibrium vapor pressures of all alloying elements add up to 1 atmosphere. Figure 6C and D show the equilibrium vapor pressures of the various alloying elements over 304 stainless steel and the total equilibrium vapor pressures over the two liquid

alloys 204 and 304 stainless steels, respectively. In calculating the equilibrium vapor pressures over the alloys, it was assumed that the metallic solutions behaved ideally and their activities were equal to their respective mole fractions. The boiling point of the two alloys were found to be 2844 and 3051 K for 204 and 304 stainless steels, respectively.

Figure 7 shows the computed temperature field and vapor flux on the top surface of the weld pool. As can be seen, the spatial distribution of vapor fluxes is similar to that of the temperature profiles with larger fluxes originating from regions of higher temperatures. The temperature inside the keyhole is slightly higher than the boiling temperature of the alloy and decreases sharply outside the keyhole from 2844 to 2200 K in a small circular region of approximately 0.3 mm diameter. Since the temperature outside the keyhole is lower than the boiling temperature of the alloy, the vapor fluxes driven by the concentration gradient are much lower than the fluxes from inside the keyhole, which is shown in Fig. 7B and C. As anticipated, the vaporization is most pronounced in the keyhole zone. The total vapor flux from the keyhole is larger than that from outside the keyhole because of the large internal surface area of the keyhole and the pressure driven flux.

Figure 8 shows the typical concentration profiles of manganese and

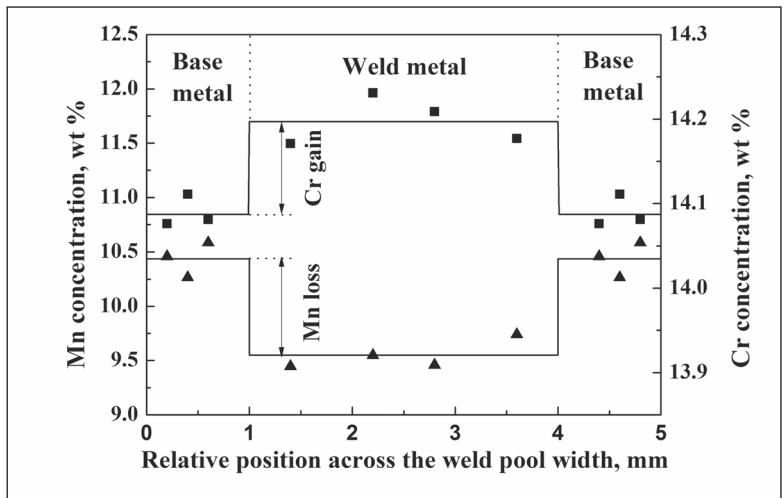


Fig. 8 — Concentration profiles of manganese and chromium across the fusion zone in the transverse section of 204 stainless steel weld. The solid line is the computed result. $P = 1250\text{ W}$, $v = 8\text{ mm s}^{-1}$.

chromium along a horizontal monitoring line across the transverse section of the weld. The concentration of manganese decreases significantly in the fusion zone compared with that in the based metal. The loss of manganese concentration is consistent with the high equilibrium vapor pressure shown in Fig. 6B. Apart from the usual scatter, the decrease in manganese concentration in the fusion zone does not show any trend of spatial variation, which indicates that the weld pool was well mixed because of the recirculating flow of the liquid metal.

An interesting feature of Fig. 8 is that the concentration of chromium in weld metal is higher than that in the base metal. Although chromium vaporizes during welding, more pronounced loss of mass of the other alloying elements, particularly iron, results in an increase of chromium concentration. This behavior is consistent with the mass balance expressed by Equation 8, which indicates that the concentration of an element may increase because of the more pronounced loss of other alloying elements. Similarly, a small increase in the concentrations of nickel and iron can be observed in Fig. 9.

The calculated changes in composition of the various alloying elements agree well with the corresponding measured values. In the high-manganese stainless steel, the concentration of manganese decreases by about 1.3 wt-% for a laser power of 1250 W.

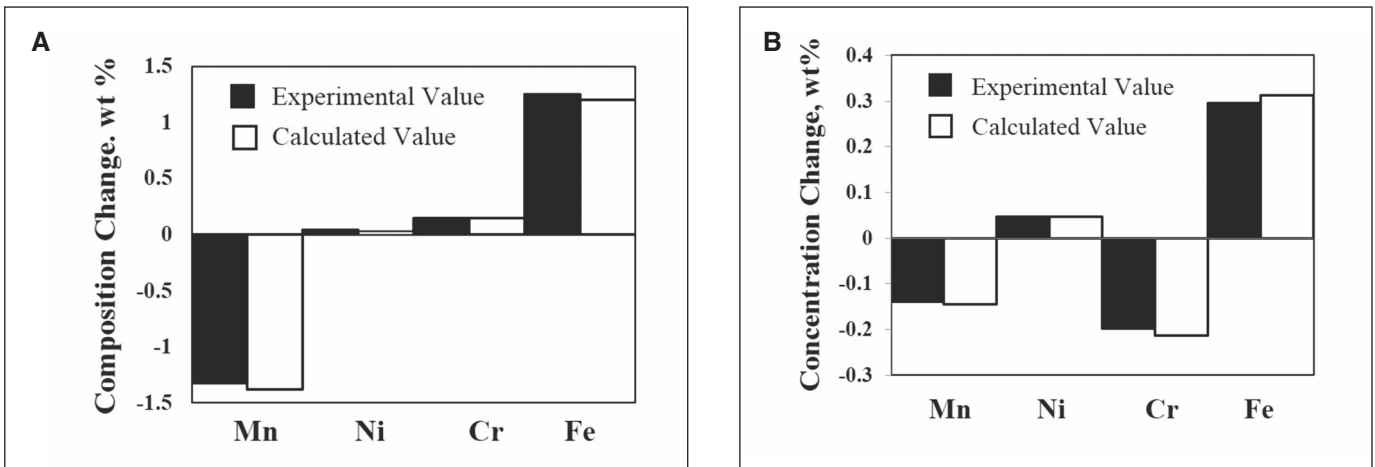


Fig. 9 — Comparison of the calculated and the experimentally determined composition change at a laser power of 1250 W and welding speed of 8 mm/s for the following: A — 204 stainless steel ; B — 304 stainless steel.

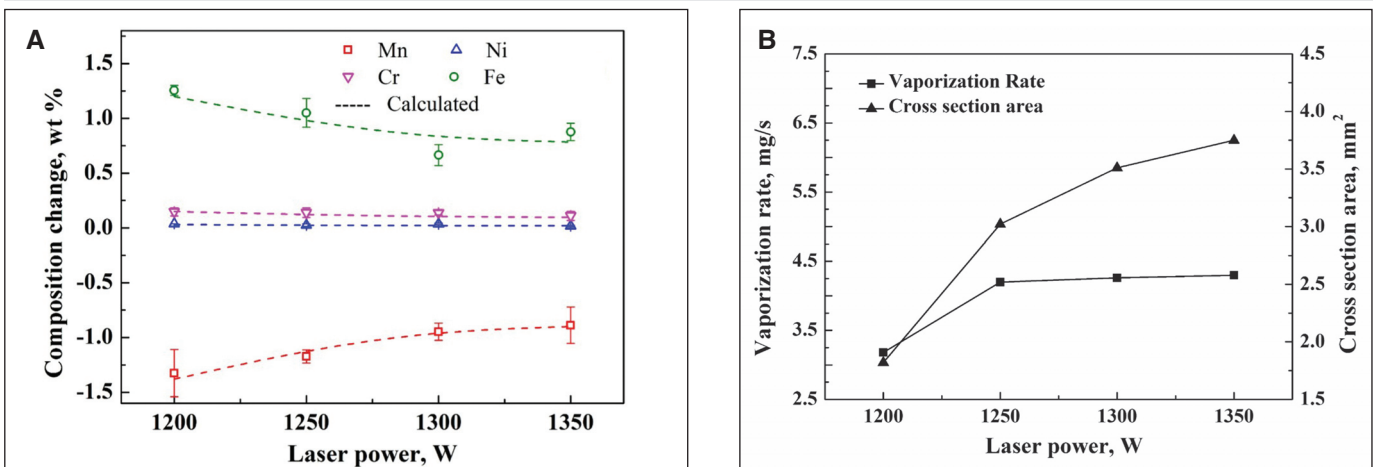


Fig. 10 — Influence of laser power on the following: A — Composition change; B — vaporization rate and transverse cross section area of the fusion zone during laser welding of 204 stainless steel at a welding speed of 8 mm s⁻¹.

The concentrations of chromium and iron increase by about 0.2 and 1.2 wt%, respectively. The change in the concentration of nickel was insignificant, indicating that the loss of nickel was similar in proportion to the overall loss of all alloying elements by vaporization.

Figure 9 shows the comparison of the alloying element loss in the two stainless steel welds with different manganese concentrations. As anticipated, the decrease in the concentration of manganese was much more pronounced in 204 stainless steel than that in 304 stainless steel because of the difference in the manganese concentrations of the two steels. All alloying elements are lost from both steels during welding. However, the extent of loss of an individual alloying element such as chromium relative to the

total loss of all alloying elements determine its concentration in the weld metal.

Although the change in the concentration of chromium was small in both steels, its concentration decreased in 304 whereas the chromium concentration was slightly higher than that in the 204 steel base metal. The total rate of vaporization of all alloying elements was much more pronounced in the 204 stainless steel. Furthermore, the vaporization rate of chromium was more pronounced from the 304 stainless steel because of its higher concentration in this steel. The higher vaporization rate of chromium compared with the total vaporization rate of all alloying elements resulted in a loss of chromium concentration in 304 stainless steel. In contrast, in 204 stainless steel, the vaporization rate of chromi-

um was lower than that from 304 steel. In addition, the overall vaporization rate from 204 steel was higher than that from 304. As a result, the chromium concentration showed a decrease in the weld metal.

Influence of Welding Parameters

Figure 10A shows the influence of laser power on the composition change of 204 stainless steel. The experimental data show considerable decrease of manganese concentration in all laser powers in the range of 1200 to 1350 W. The change in concentration of manganese is slightly higher at lower laser power. It is instructive to review the causative factors for this behavior based on Equation 8, which shows that the composition change is

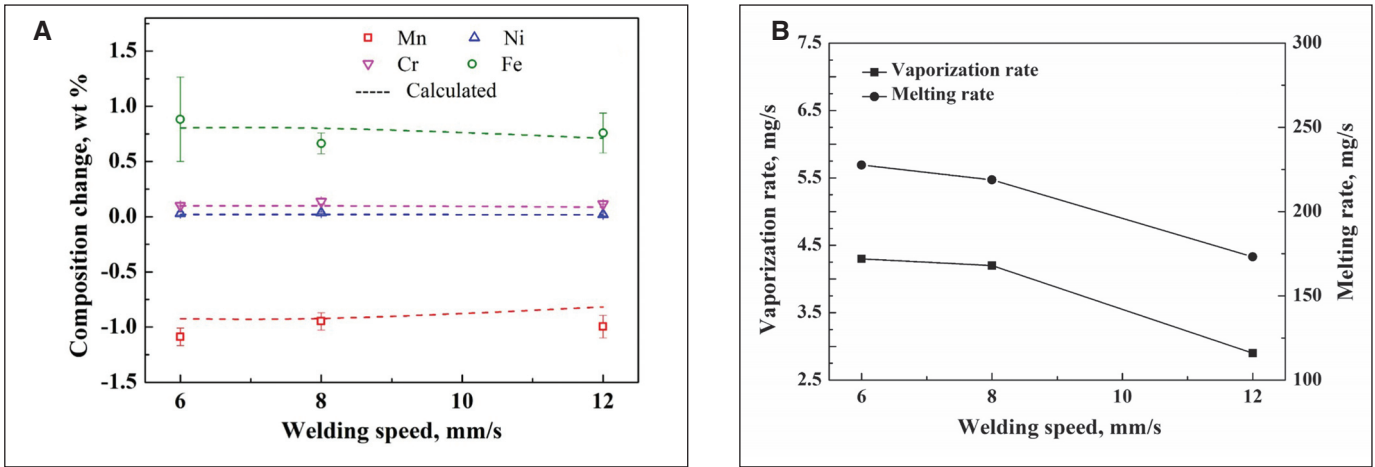


Fig. 11 — Influence of welding speed on the following; A — Composition change; B — vaporization rate and melting rate during laser welding of 204 stainless steel for a laser power of 1300 W.

affected by the vaporization rate and the melting rate from which the vapors are lost.

At a constant welding speed, the melting rate is the product of density, ρ , the welding speed, v , and the area of the transverse cross section of the fusion zone, A . Both the vaporization rate and the area of the fusion zone in the transverse section increases with the increase in laser power from 1200 to 1250 W. The mode of welding changes from partial to complete joint penetration and both the keyhole and the weld pool become deeper and wider.

Figure 10B shows that when the laser power increases from 1250 to 1350 W, the cross section area increases while the vaporization rate does not change significantly due to the insignificant change of the keyhole size — Fig. 4. Therefore, in this power range, the composition change becomes less pronounced as the laser power increases as shown in Fig. 10A.

As shown in Fig. 11A, the influence of welding speed on the composition change of 204 stainless steel is negligible. The variation of melting rate and the vaporization rates with welding speed are plotted in Fig. 11B because they are important in determining the composition change as indicated by Equation 8. It can be observed that both the vaporization and melting rates decrease with the increase in welding speed. The vaporization rates are higher for complete joint penetration welds at welding speeds of 6 and 8 mm s⁻¹ than for the partial joint penetration welds at a welding speed of 12 mm s⁻¹. The key-

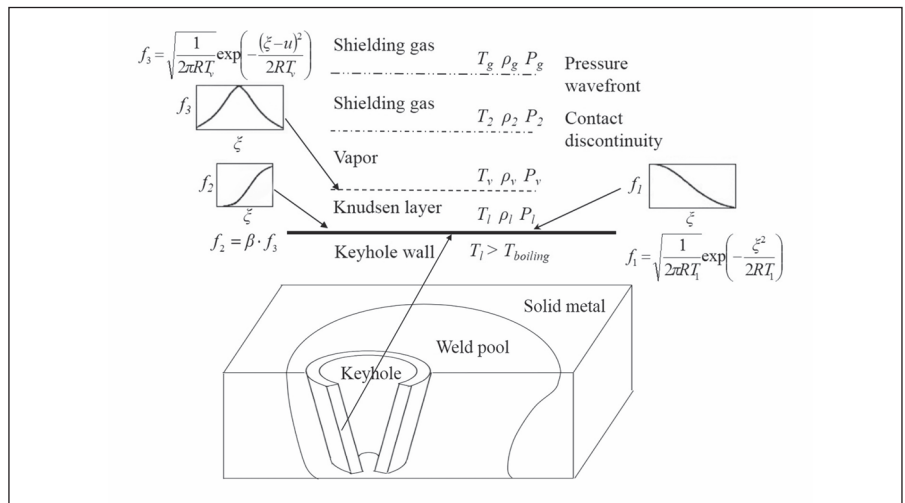


Fig. 12 — Schematic diagram of the velocity distribution functions in the Knudsen layer and in adjacent regions. $T_{boiling}$ is the boiling temperature of the alloy; $T_l, \rho_l,$ and P_l are the temperature, density, and pressure of the vapor on the liquid surface, respectively; $T_v, \rho_v,$ and P_v are the temperature, density, and pressure of the vapor at the edge of the Knudsen layer, respectively; $T_2, \rho_2,$ and P_2 are the temperature, density, and pressure of the vapor behind the wavefront, respectively; and $T_g, \rho_g,$ and P_g are the temperature, density, and pressure of the vapor in front of the wavefront, respectively. R is the gas constant, ξ is the velocity component normal to the vaporizing surface, u is the mean velocity of the local gas, and β is the proportionality coefficient.

hole size is significantly larger in complete joint penetration welds as shown in Fig. 4. Furthermore, the higher welding speed reduces the cross section area of the fusion zone as shown in Fig. 5. As a result, the composition change is not significantly affected by the welding speed.

Summary and Conclusions

Loss of alloying elements because of vaporization and the resulting composition change of the weld metal during keyhole mode laser welding of two

stainless steels were examined experimentally and theoretically. Concentration profiles of alloying elements in the welds were determined for both partial and complete joint penetration welds. A well-tested numerical model was used to compute the keyhole and weld pool geometry and the temperature fields for various laser powers and welding speeds. These simulations were combined with a model developed to calculate weld composition change based on the principles of transport phenomena, kinetics, and thermodynamics. The good agreement of the composition

change of alloying elements between the calculated result and the corresponding experimental data indicates that this model is capable of predicting composition change in keyhole mode laser welding for various conditions. The main conclusions are as follows:

1. In all cases of partial and complete joint penetration keyhole mode linear welding of two stainless steels, the shape, size and the internal surface area of the keyhole, the surface area of the molten pool, and the temperature field affected the vaporization rates of all alloying elements. These variables were affected by the laser power, power density, and the welding speed. The change in the composition of the weld metal was affected by the relative rates of vaporization of various alloying elements and the melting rates of the base metal. Because of the interdependence of many variables, the role of welding variables on the final chemical composition of the alloying elements could not be predicted intuitively. However, the proposed computational model could correctly predict the roles of laser power and welding speed on the composition changes.

2. An increase in laser power keeping the welding speed constant resulted in an expected larger weld pool and higher rates of vaporization of alloying elements. However, the faster vaporization did not result in more pronounced changes in composition since the vaporization of alloying elements affected the chemical composition of a significantly larger volume of weld metal at higher laser powers. Higher laser power resulted in lower composition change of alloying elements due to the significant increase of the melting rate compared with the modest increase of the vaporization rate.

3. Higher welding speed resulted in both a lower vaporization rate and a reduced melting rate for both partial and complete joint penetration welds. The composition change was not sensitive to the welding speed because of the compensating effects of these two parameters.

4. Vaporization of iron, chromium, manganese, and nickel took place from the keyhole for partial and complete joint penetration welds for both 204 and 304 stainless steels. Pronounced vaporization of iron and chromium occurred for all laser powers and welding

speeds investigated for both steels. Rate of vaporization of manganese was much higher for 204 stainless steel than for 304 steel.

5. The vaporization of alloying elements from the keyhole was driven by both concentration and pressure gradients while outside the keyhole the rates of vaporization were influenced by the concentration gradients of metal vapors.

6. As expected, pronounced vaporization of alloying elements occurred for both partial and complete joint penetration welds mainly from the keyhole due to high local temperatures. A keyhole wall temperature of about 10 K higher than the boiling points of the alloys could correctly explain the rates of vaporization of alloying elements for both alloys studied in partial and complete joint penetration keyhole welds.

7. The concentration of manganese in the weld metal was significantly lower than that in the base metal for the welding of 204 stainless steel mainly because of its high concentration of manganese. In contrast, for the welding of 304 stainless steel, the decrease in the concentration of chromium in the weld metal was greater than that of manganese. Because of the higher boiling point and higher concentration of chromium in 304 than 204 stainless steel, the loss of chromium was more pronounced in 304 stainless steel.

Acknowledgments

The authors would like to thank S. L. Gao and R. X. Yang for performing the laser welding experiments, as well as James S. Zuback for assisting with the metallography. This research was supported by the Natural Science Foundation of Tianjing (grant no. 16JCZDJC38700).

References

- Zhan, X., Chen, J., Liu, J., Wei, Y., Zhou, J., and Meng, Y. 2016. Microstructure and magnesium burning loss behavior of AA6061 electron beam welding joints. *Materials & Design* 99: 449–458.
- Anisimov, S. I., and Rakhmatulina, A. K. 1973. The dynamics of the expansion of a vapor when evaporated into a vacuum.

Soviet Physics — JETP 37(3): 441–444.

3. Knight, C. J. 1982. Transient vaporization from a surface into vacuum. *AIAA Journal* 20(7): 950–954.

4. Knight, C. J. 1979. Theoretical modeling of rapid surface vaporization with back pressure. *AIAA Journal* 17(5): 519–523.

5. Mundra, K., and DeRoy, T. 1993. Calculation of weld metal composition change in high-power conduction mode carbon-dioxide laser-welded stainless-steels. *Metallurgical Transactions B* 24(1): 145–155.

6. Zhao, H., and DeRoy, T. 2001. Weld metal composition change during conduction mode laser welding of aluminum alloy 5182. *Metallurgical and Materials Transactions B* 32(1): 163–172.

7. He, X., DeRoy, T., and Fuerschbach, P. W. 2003. Alloying element vaporization during laser spot welding of stainless steel. *Journal of Physics D—Applied Physics* 36(23): 3079–3088.

8. He, X., DeRoy, T., and Fuerschbach, P. W. 2003. Probing temperature during laser spot welding from vapor composition and modeling. *Journal of Applied Physics* 94(10): 6949–6958.

9. Khan, P. A. A., and DeRoy, T. 1984. Alloying element vaporization and weld pool temperature during laser-welding of Aisi 202 stainless-steel. *Metallurgical Transactions B* 15(4): 641–644.

10. Mundra, K., and DeRoy, T. 1993. Toward understanding alloying element vaporization during laser beam welding of stainless steel. *Welding Journal* 72(1): 1-s to 9-s.

11. Collur, M. M., and DeRoy, T. 1989. Emission-spectroscopy of plasma during laser-welding of Aisi-201 stainless-steel. *Metallurgical Transactions B* 20(2): 277–286.

12. Collur, M. M., Paul, A., and DeRoy, T. 1987. Mechanism of alloying element vaporization during laser-welding. *Metallurgical Transactions B* 18(4): 733–740.

13. Sahoo, P., Collur, M. M., and DeRoy, T. 1988. Effects of oxygen and sulfur on alloying element vaporization rates during laser-welding. *Metallurgical Transactions B* 19(6): 967–972.

14. Dilthey, U., Goumeniouk, A., Lopota, V., Turichin, G., and Valdaitseva, E. 2001. Development of a theory for alloying element losses during laser beam welding. *Journal of Physics D—Applied Physics* 34(1): 81–86.

15. Jandaghi, M., Parvin, P., Torkamany, M. J., and Sabbaghzadeh, J. 2008. Alloying element losses in pulsed Nd: YAG laser welding of stainless steel 316. *Journal of Physics D: Applied Physics* 41(23): 235503.

16. Jandaghi, M., Parvin, P., Torkamany, M. J., and Sabbaghzadeh, J. 2009. Measurement of the composition change in Al5754 alloy during long pulsed Nd: YAG laser weld-

ing based on LIBS. *Journal of Physics D: Applied Physics* 42(20): 205301.

17. Bag, S., Trivedi, A., and De, A. 2008. Use of a multivariate optimization algorithm to develop a self-consistent numerical heat transfer model for laser spot welding. *The International Journal of Advanced Manufacturing Technology* 38(5-6): 575-585.

18. Rai, R., Elmer, J. W., Palmer, T. A., and DebRoy, T. 2007. Heat transfer and fluid flow during keyhole mode laser welding of tantalum, Ti-6Al-4V, 304L stainless steel and vanadium. *Journal of Physics D: Applied Physics* 40(18): 5753-5766.

19. Rai, R., Kelly, S. M., Martukanitz, R. P., and DebRoy, T. 2008. A convective heat-transfer model for partial and full penetration keyhole mode laser welding of a structural steel. *Metallurgical and Materials Transactions A* 39(1): 98-112.

20. Rai, R., Roy, G. G., and DebRoy, T. 2007. A computationally efficient model of convective heat transfer and solidification characteristics during keyhole mode laser welding. *Journal of Applied Physics* 101(5): 054909.

21. Ribic, B., Rai, R., and DebRoy, T. 2008. Numerical simulation of heat transfer and fluid flow in GTA/Laser hybrid welding. *Science and Technology of Welding and Joining* 13(8): 683-693.

22. Ribic, B., Tsukamoto, S., Rai, R., and DebRoy, T. 2011. Role of surface-active elements during keyhole-mode laser welding. *Journal of Physics D: Applied Physics* 44(48): 485203.

23. Schlunder, E., and Gnielinski, V. 1967. Heat and mass transfer between surfaces and impinging jets. *Chemie Ingenieur Technik* 39: 578-584.

24. Zhao, H., and DebRoy, T. 2003. Macroporosity free aluminum alloy weldments through numerical simulation of keyhole mode laser welding. *Journal of Applied Physics* 93(12): 10089-10096.

25. Rai, R., Burgardt, P., Milewski, J. O., Lienert, T. J., and DebRoy, T. 2009. Heat transfer and fluid flow during electron beam welding of 21Cr-6Ni-9Mn steel and Ti-6Al-4V alloy. *Journal of Physics D: Applied Physics* 42(2): 025503.

26. Honig, R. E., and Kramer, D. A. 1970. *Physicochemical Measurements in Metal Research*. 505, New York, NY, Interscience Publishers.

27. Hultgren, R., Desai, P. D., Hawkins, D. T., Gleiser, M., Kelley, K. K., and Wagman, D. D. 1973. *Selected Values of the Thermodynamic Properties of the Elements*. Materials Park, Ohio, ASM International.

28. Yaws, C. L. 1994. *Handbook of Vapor Pressure*. Houston, Tex., Gulf Publishing Co.

29. Alcock, C. B., Itkin, V. P., and Horrigan, M. K. 1984. Vapor pressure equations for the metallic elements. *Canadian Metallurgical Quarterly* 23(3): 309-313.

Appendix A

1. Keyhole Geometry

The keyhole geometry was calculated from local heat balance on the keyhole wall where temperature is assumed to be the boiling point of the alloy (Ref. 24). Since the orientation of the keyhole is almost vertical, the heat transfer occurred mainly along the horizontal plane. The local keyhole wall angle with the vertical direction θ is given by (Refs. 24, 25):

$$\tan(\theta) = \frac{I_c}{I_a - I_v} \quad (A1)$$

where I_c is the heat flux conducted into the keyhole wall, I_a is the locally absorbed beam energy flux, and I_v is the evaporative heat flux on the keyhole wall. The value of I_c is calculated from a two-dimensional temperature field in an infinite plate with the line heat source (Ref. 24):

$$I_c(r, \varphi) = -\lambda \frac{\partial T(r, \varphi)}{\partial r} \quad (A2)$$

where (r, φ) indicates a location in the plate with the line source as the origin, T is the temperature, and λ is the thermal conductivity. The two-dimensional temperature field, $T(r, \varphi)$, can be calculated conduction heat from the keyhole wall into the plate (Ref. 24):

$$T(r, \varphi) = T_a + \frac{P'}{2\pi\lambda} K_0(\Omega r) e^{-\Omega r \cos\varphi} \quad (A3)$$

where T_a is the ambient temperature, P' is the power per unit depth, $K_0(\cdot)$ is the zero-order second kind modified Bessel function, and $\Omega = v/(2\kappa)$, where v is the welding speed and κ is the thermal diffusivity.

The locally absorbed beam energy flux, I_a , on the keyhole wall is obtained by considering the Fresnel absorption during multiple reflections and the plasma absorption (Ref. 24):

$$I_a = e^{-\beta L} \left(1 - (1 - \alpha)^{1 + \pi/4\bar{\theta}} \right) I_0 \quad (A4)$$

where β is the plasma attenuation coefficient, L is the average path of the laser beam in plasma before it reaches the keyhole wall, α is the absorption coefficient of the workpiece, $\bar{\theta}$ is the

average angle between the keyhole wall and the initial incident beam axis, and I_0 is the local beam intensity, which varies with depth from the surface and radial distance from the beam axis, and given by (Ref. 24):

$$I_0 = I_p \left(\frac{r_0}{r_f} \right)^2 \exp \left(-\frac{r^2}{r_f^2} \right) \quad (A5)$$

where I_p is the peak intensity at the focal point, given by $2P/(\pi r_0^2)$, P is the laser power, r_0 is the beam radius at the focal point, and r_f is the local beam radius, which is calculated by (Ref. 24):

$$r_f = r_0 \left(1 + \left(\frac{z + z_0}{2r_0 l / d_b} \right)^2 \right)^{1/2} \quad (A6)$$

where z , and z_0 , are the depth and the beam defocusing, respectively. l is the beam focal length, and d_b is the beam diameter on the laser focusing lens.

The vaporization flux, I_v , on the keyhole wall is obtained from Ref. 24:

$$I_v = \sum_{i=1}^n J_i \Delta H_i \quad (A7)$$

where J_i is the vaporization flux of element i , ΔH_i is the heat of vaporization of element i , and n is the total number of alloying elements in the alloy. For simplicity, the vaporization flux of element i was calculated by using the Langmuir equation (Refs. 12, 13)

$$J_i = \frac{P_i}{7.5} \sqrt{\frac{M_i}{2\pi RT_b}} \quad (A8)$$

where P_i is the vapor pressure of element i over the alloy, M_i is the molecular weight of element i , T_b indicates the boiling temperature of the alloy, and R is the gas constant. The factor 7.5 accounts for lower vaporization rates at 1 atmosphere pressure compared with that in vacuum-based experiments.

The keyhole profile was calculated for various horizontal planes from top to bottom. Initially, on the top surface, the local angles of the front and rear walls of the keyhole were calculated from Equation A1. The asymmetric keyhole boundary was determined by both a maximum x value and a minimum x value for each y value where x is the welding direction and y is the width direction. The keyhole wall positions in

the plane right below the top surface could be calculated from the current positions and the local angles. Similarly, the keyhole positions in various planes downward were determined. Using the calculated position of front and rear walls of the keyhole, the strength of the line source P' at any given depth were calculated. Using the calculated strength and the location of the line source, the temperature field in the x-y plane at each depth were determined. Subsequently the temperature field of the entire calculation domain was computed considering the energy transferred from the keyhole wall. The temperature and velocity fields in the vapor within the keyhole were not calculated. Heat transfer and fluid flow in the base plate outside the keyhole was computed as follows.

2. Heat Transfer and Fluid Flow in the Weld Pool

The temperature and velocity fields in the liquid region and the temperature field in the solid region were calculated by solving the equations of conservation of mass, momentum, and energy in three dimensions. It is assumed that the molten metal is incompressible, laminar, and Newtonian fluid. The momentum conservation equation of the fluid flow in the weld pool is given as (Ref. 19):

$$\rho \frac{\partial u_j}{\partial t} + \rho \frac{\partial(u_i u_j)}{\partial x_i} = \frac{\partial}{\partial x_i} \left(\mu \frac{\partial u_j}{\partial x_i} \right) + S_j \tag{A9}$$

where ρ is the density, t is the time, x_i is the distance along the i th ($i = 1, 2,$ and 3) orthogonal direction, u_j is the velocity component along the j direction, μ is the effective viscosity, and S_j is the source term for the j th momentum, equation due to frictional dissipation in the mushy zone, buoyancy source, and the relative motion between the laser source and the workpiece.

The pressure field can be obtained by solving the momentum equation in conjunction with the following continuity equation (Ref. 19):

$$\frac{\partial(\rho u_i)}{\partial x_i} = 0 \tag{A10}$$

The thermal energy transportation in the weld workpiece can be ex-

pressed by the following modified energy equation (Ref. 19):

$$\rho \frac{\partial h}{\partial t} + \rho \frac{\partial(u_i h)}{\partial x_i} = \frac{\partial}{\partial x_i} \left(\frac{k}{C_p} \frac{\partial h}{\partial x_i} \right) + S_h \tag{A11}$$

where k is the thermal conductivity, and S_h is the source term due to the latent heat content. The calculation process of the source term S_j and S_h is well documented in the literature (Refs. 18–20), and not discussed here.

3. Boundary Conditions

The calculation is based on a 3D Cartesian coordinate system. Since the weld is symmetrical about the centerline, only half of the workpiece is considered. Further discussion of the boundary conditions are represented as follows:

A. *Top surface* — On the top surface, the weld pool except the keyhole region is assumed to be flat. The velocity components along the x and y directions, u and v , are determined from the Marangoni effect. However, the velocity components along the z direction, w , is 0 due to the negligible outward flow at the top surface. Therefore, the velocity boundary condition can be obtained as the following equations:

$$\begin{cases} \mu \frac{\partial u}{\partial z} = f_L \frac{d\gamma}{dT} \frac{\partial T}{\partial x} \\ \mu \frac{\partial v}{\partial z} = f_L \frac{d\gamma}{dT} \frac{\partial T}{\partial y} \\ w = 0 \end{cases} \tag{A12}$$

where f_L is the liquid fraction, and $d\gamma/dT$ is the temperature coefficient of surface tension.

The heat flux at the top surface can be derived from the heat input, which follows a Gaussian heat distribution, the heat loss by radiation, and the heat loss by convection. The expression is given as follows:
given as:

$$k \frac{\partial T}{\partial z} \Big|_{top} = \frac{fQ\eta}{\pi r_b^2} \exp\left(-\frac{f(x^2 + y^2)}{r_b^2}\right) - \sigma \epsilon (T^4 - T_a^4) - h_c (T - T_a) \tag{A13}$$

where r_b is the beam radius, f is the power distribution factor, Q is the total laser power, η is the absorptivity, σ is the Stefan–Boltzmann constant, h_c is the heat-transfer coefficient, and T_a is the ambient temperature.

B. *Symmetric plane* — The velocity components and heat flux along the y direction across the symmetric surface are zero. As a result, the boundary conditions can be defined as:

$$\begin{cases} \frac{\partial u}{\partial y} = 0 \\ v = 0 \\ \frac{\partial w}{\partial y} = 0 \\ \frac{\partial h}{\partial y} = 0 \end{cases} \tag{A14}$$

C. *Keyhole surface* — In this model, mass flux due to convection at the keyhole surface is neglected. As a result, the velocity components perpendicular to the keyhole surface are assigned 0. Since the temperature of the keyhole wall is treated as boiling point of the alloy, h is equal to the sensible heat of the boiling temperature:

$$h = h_{boil} \tag{A15}$$

D. *Bottom surface* — For partial joint penetration welds, the velocities are zero at the bottom surface, and the convective heat transfer is considered as the boundary condition. For complete joint penetration welds, the velocity boundary conditions are similar with that at the top surface under the Marangoni effect, and are given as the following:

$$\begin{cases} \mu \frac{\partial u}{\partial z} = f_L \frac{d\gamma}{dT} \frac{\partial T}{\partial x} \\ \mu \frac{\partial v}{\partial z} = f_L \frac{d\gamma}{dT} \frac{\partial T}{\partial y} \\ w = 0 \end{cases} \tag{A16}$$

E. *Solid surfaces* — The velocities

are set to be 0, and the temperatures are set at ambient temperature at all solid surfaces far away from the heat source.

Appendix B

Vapor Flux Due to Pressure Gradient

For welding at atmospheric pressure, when the local temperature on the liquid surface exceeds the boiling point of the alloy, the local equilibrium pressure exceeds the ambient pressure and vaporization occurs due to pressure gradient. Knight (Ref. 4) derived a set of equations that describe the vaporization rate under these conditions. The derivation of these equations is not repeated here. Instead, the salient features and the final expressions are indicated.

The vapor molecules that escape from the liquid surface, their only path is away from the liquid. As a result, the velocity distribution function is half-Maxwellian as shown schematically in Fig. 12.

In the Knudsen layer, which is a thin layer close to the interface having a thickness of a few mean-free paths, the velocity distribution can vary from $-\infty$ to $+\infty$. Many of the molecules that vaporize from the surface, recondense back on the surface and the net vaporization rate is the difference between the two rates. Based on these concepts, the temperature T_v , the density ρ_v , the pressure P_v , and the mean velocity u of the vapor at the edge of the Knudsen layer can be related to the temperature T_l , density ρ_l , and pressure P_l of the vapor on the liquid surface. The derived jump conditions across the Knudsen layer are given (Refs. 2, 4):

$$\frac{T_v}{T_l} = \left[\frac{\sqrt{1 + \pi \left(\frac{\gamma_v - 1}{\gamma_v + 1} \frac{m}{2} \right)^2}}{-\sqrt{\pi} \frac{\gamma_v - 1}{\gamma_v + 1} \frac{m}{2}} \right]^2 \quad (B1)$$

Table 4 — Equilibrium Vapor Pressures of Various Elements in Atmospheres as a Function of Temperature in K (Refs. 26–29)

Mn	$\log P^0 = -5.58 \times 10^{-4} T - 1.503 \times 10^{-4} / T + 16.615$
Ni	$\log P^0 = 6.666 - 20765 / T$
Cr	$\log P^0 = 13.505 \times 10^3 / T + 33.65 \log T - 9.29 \times 10^{-3} T + 8.381 \times 10^{-7} T^2 - 91.083$
Fe	$\log P^0 = 11.5549 - 1.9538 \times 10^4 / T - 0.62549 \log T - 2.7182 \times 10^{-9} T + 1.9086 \times 10^{-13} T^2 - 2.881$

$$\frac{\rho_v}{\rho_l} = \sqrt{\frac{T_l}{T_v}} \left[\left(m^2 + \frac{1}{2} \right) e^{m^2} \operatorname{erfc}(m) - \frac{m}{\sqrt{\pi}} \right] + \frac{1}{2} \frac{T_l}{T_v} \left[1 - \sqrt{\pi} m e^{m^2} \operatorname{erfc}(m) \right] \quad (B2)$$

$$\beta = \left[(2m^2 + 1) - m \sqrt{\pi} \frac{T_l}{T_v} \right] e^{m^2} \frac{\rho_l}{\rho_v} \sqrt{\frac{T_l}{T_v}} \quad (B3)$$

where the dimensionless velocity, m , is given by $m = u / \sqrt{2R_v T_v}$, $R_v = R / M_v$, R is the gas constant, M_v is the average molecular weight of the vapor, γ_v is the ratio of specific heat of the vapor, which is treated as a monatomic gas ($\gamma_v = 5/3$), erfc is the complementary error function, $\operatorname{erfc}(m) = (2/\sqrt{\pi}) \int_m^\infty e^{-v^2} dv$, and β is the condensation factor. The equilibrium vapor pressure P_l at the interface is obtained from the equilibrium vapor pressure-temperature relationship of the various alloying elements:

$$P_l = \sum_{i=1}^n P_i = \sum_{i=1}^n a_i P_i^0 \quad (B4)$$

where P_i is the equilibrium vapor pressure of element i over the alloy, a_i is the activity of the element i in the liquid metal, which is determined by its concentration in the weld pool. In this calculation, the mole fraction of the element i was used as the value of a_i because alloys behave ideally close to their boiling points. P_i^0 is the equilibrium vapor pressure of element i over pure liquid, and n is the number of alloying elements. The equations used to calculate P_i^0 are presented in Table 4.

The average molecular weight of the vapor, M_v , is given by:

$$M_v = \sum_i^n M_i \frac{a_i P_i^0}{P_l} \quad (B5)$$

where M_i is the molecular weight of element i .

The relationship of the pressure at the edge of the Knudsen layer and the ambient conditions is obtained by applying the Rankine-Hugoniot relation:

$$\frac{P_l}{P_g} \frac{P_2}{P_l} = 1 + \gamma_g M \Gamma \left[\frac{\gamma_g + 1}{4} M \Gamma + \sqrt{1 + \left(\frac{\gamma_g + 1}{4} M \Gamma \right)^2} \right] \quad (B6)$$

where P_g and P_2 are the pressures in front of and behind the wavefront, respectively, $P_2 = P_v$, γ_g is the ratio of the specific heats for the shielding gas, $\Gamma = \sqrt{\gamma_v R_v T_v} / \sqrt{\gamma_g R_g T_g}$, and M is the Mach number, which is related to dimensionless velocity, m , by the equation:

$$m = M \sqrt{\frac{\gamma_v}{2}} \quad (B7)$$

The Mach number M and the density ρ_l , obtained by solving equations B1–7, can be used to calculate the vaporization flux. The unknown variable, u , can be obtained by solving these equations. J_p , owing to the pressure gradient on the keyhole wall surface as follows:

$$J_p = \rho_v M S \quad (B8)$$

where S is the speed of sound in the vapor at temperature T_v .

T. LIU, L. J. YANG, and W. C. QIU are with the School of Materials Science and Engineering, Tianjin University, Tianjin, China. T. LIU, H. L. WEI and T. DEBROY (debroy@psu.edu) are with the Department of Materials Science and Engineering, Pennsylvania State University, University Park, Pa.